UAV-based semi-airborne CSEM for mineral exploration - 3D joint inversion of scalar and vector magnetometer data

Raphael Rochlitz[1], Philipp Kotowski[2], Thomas Günther[1] and Michael Becken[2]

[1]Leibniz Institute for Applied Geophysics, LIAG, Hanover, Germany

[2]University of Münster, WWU, Münster, Germany

Summary

We performed drone-based semi-airborne electromagnetic (EM) measurements in an active mining area in the Eastern part of the Iberian pyrite belt, Spain. The area is poorly accessible and features rough terrain with height undulations up to 400 m. Using drones as carrier for magnetic field receivers offered areal accessibility as a cost-effective alternative to helicopter-towed EM systems with simplified logistics. We analyzed data in two overlapping frequency ranges, 1-128 Hz and 30-1024 Hz, recorded with a scalar and a vector magnetic field receiver, respectively. We added capabilities to invert both data sets jointly with the open-source 3D inversion tools custEM/pyGIMLi and discuss the results using this procedure compared to single-dataset inversion.

Keywords: Controlled-source, Electromagnetic Theory, Semi-airborne, 3D inversion, UAV

Introduction

Within the last decades, electromagnetic geophysical methods were continuously developed and have shown to be indispensable for the exploration of mineral deposits, hydrocarbon reservoirs, groundwater or geothermal resources, and others. Amongst them, semi-airborne electromagnetic (EM) surveys have recently received renewed interest. They combine the advantages of fast data collection using airborne receivers (Rx) and strong signals emitted by ground-based transmitters (Tx). For instance, Mogi et al. (2009) show that penetration depths of several hundreds down to 1000 meters can be reached with such setups while covering multiple square-kilometers of area.

Becken et al. (2020) presents the DESMEX system analyzing the recorded EM data in the frequency domain. Meanwhile, the rapid development of UAVs (Figure 1) as carriers for geophysical equipment allowed a transition from helicopter-towed Rx to UAV-towed Rx with significantly reduced costs and simpler logistics. In the most recent years, working groups around the globe developed different controlled-source EM systems (Q. Wu et al., 2019; Vilhelmsen & Døssing, 2022; Bastani & Joahansson, 2022; J. Wu et al., 2023). Becken et al. (2022) present a new measurement system for mineral exploration using a scalar optically pumped magnetometer (*MagArrow*). We performed a second survey with an equivalent setup in cooperation with Sandfire MATSA in the active mining area of the Eastern Iberian pyrite belt, Spain and used in addition a second vector magnetic field receiver introduced by Kotowski et al. (2022), the *SHFT* sensor. We refer to the scalar and vector sensors as SM and VM.

The two different receivers complement each other well being sensitive below 256 Hz (SM) and above 32 Hz (VM). For the inversion of the data, we extended the 3D open-source inversion tools based on custEM and pyGIMLi to allow on the one hand, the handling of CSEM data recorded with a SM and on the other hand, the joint inversion of multiple EM data sets. In this work, we present and discuss the inversion results of the aforementioned semi-airborne data set.

Figure 1: UAV with SHFT sensor attached in survey area north of Huelva, Spain.

Methodology

We process the data following the procedures described by Becken et al. (2020, 2022). The inversion procedure builds mainly upon the methodology presented by Grayver et al. (2013), whereat we use a finite-element discretization on unstructured tetrahedral meshes and a total electric field formulation to calculate the EM responses and corresponding sensitivities with custEM (Rochlitz et al., 2023). In this paper, we describe in detail the methodology for inverting arbitrary three-component CSEM data with a Gauss-Newton minimization approach, implemented in pyGIMLi (Rücker et al., 2017). We minimize the objective function

$$\Phi = \|\mathbf{W}_d(\mathbf{d} - \mathbf{f}(\mathbf{m}))\|_2^2 + \lambda\|\mathbf{W}_m\mathbf{m}\|_2^2 \to \min . \quad (1)$$

with the error-weighting matrix $\mathbf{W}_d$, data vector $\mathbf{d}$, forward response $\mathbf{f}(\mathbf{m})$, regularization parameter λ, and smoothness operator $\mathbf{W}_m$. To solve the minimization problem iteratively, we begin from a starting model $\mathbf{m}^0$, and update the next model $\mathbf{m}^{k+1} = \mathbf{m}^k + \tau^k\Delta\mathbf{m}^k$ with the model update $\Delta\mathbf{m}^k$ that is obtained from solving the inverse sub-problem

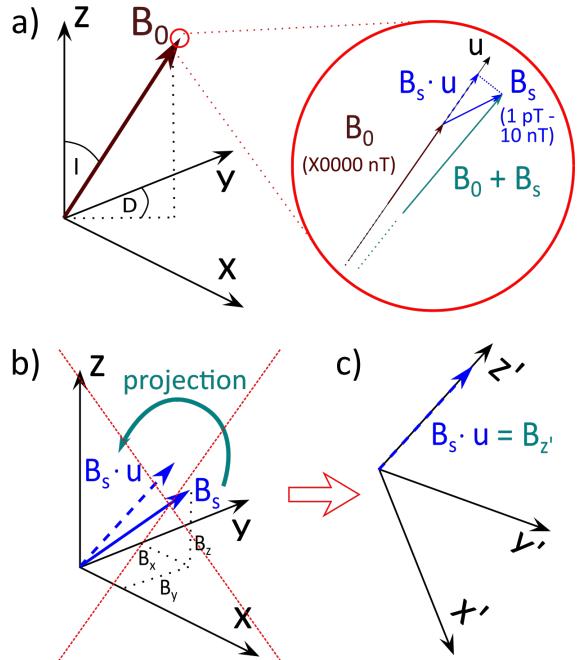$$(\mathbf{J}^T\mathbf{W}_d^T\mathbf{W}_d\mathbf{J} + \lambda\mathbf{W}_m^T\mathbf{W}_m)\Delta\mathbf{m}^k = \\ \mathbf{J}^T\mathbf{W}_m^T\mathbf{W}_m(\mathbf{d} - \mathbf{f}(\mathbf{m}^k)) - \lambda\mathbf{W}_m\mathbf{W}_m^T\mathbf{m}^k \quad (2)$$

with the sensitivity matrix $\mathbf{J}$. The step length τ^k is determined by an inexact line-search procedure that searches by linear interpolation (Günther et al., 2006).

We can use the procedure primarily developed for helicopter-based semi-airborne CSEM data directly for inverting also the UAV-based induction-coil receiver data. The 3D inversion of SM data relies on the technique described by Becken et al. (2022) for 2.5D inversion. The measured EM signal vector B superposes on the main field but leaves its direction nearly unchanged (Figure 2a). They calculate in each iteration the field component and corresponding sensitivity for a receiver-component oriented in the direction of the Earth's magnetic field (taken from the IGRF model), which requires the calculation of all three magentic field components (Figure 2b). Since the survey geometry and inversion domain discretized in the tetrahedral mesh are rotational invariant, we first rotate the complete modeling domain including Rx and Tx locations by respecting the local IGRF declination and inclination angles to align the new z' axis with the geomagnetic main field vector (Figure 2c). Now, it is only necessary to calculate the z' magnetic field component and sensitivity in each iteration, which corresponds to the field recorded by the
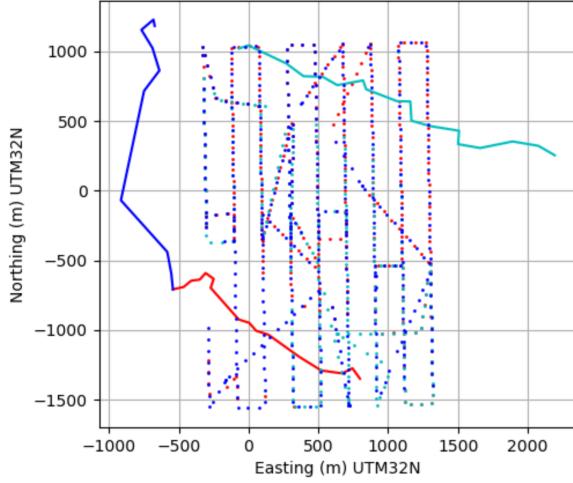
SM. Thereby, we require only one instead of three expensive sensitivity calculations for each receiver compared to the original procedure.

For all single and joint inversions, we decided to use an identical mesh to calculate the responses for the induction coil data in the earth-fixed coordinate system and for the SM data in the rotated system as described above. This procedure avoids additional interpolation steps and related errors and enables the comparison of data coverages. Methods for jointly inverting multiple EM data sets were presented by several authors (Mackie et al., 2007; Commer & Newman, 2009; Abubakar et al., 2011). Due to the similarity of the two data sets and comparable data quality, we simply stacked together the data vectors $\mathbf{d}$ in the objective function in this work. Correspondingly, the sensitivity matrices $\mathbf{J}$ of both data sets were stacked. All data points are weighted with their corresponding errors.

Figure 2: a) Geomagnetic field $\mathbf{B}_0$ described by declination $\mathbf{D}$ and inclination $\mathbf{I}$. The magnitude of the vector sum $|\mathbf{B}_0 + \mathbf{B}_s|$, with $\mathbf{B}_s$ denoting the secondary magnetic field originating from the active Tx, is approximated by its projection onto the main field, $|\mathbf{B}_0| + |\mathbf{B}_s \cdot u|$,
b) Calculating response in Cartesian coordinates and project afterwards,
c) Calculate response for $B_{z'}$ component aligned to geomagnetic field direction in a correspondingly rotated mesh; figure modified afterBecken et al. (2022).
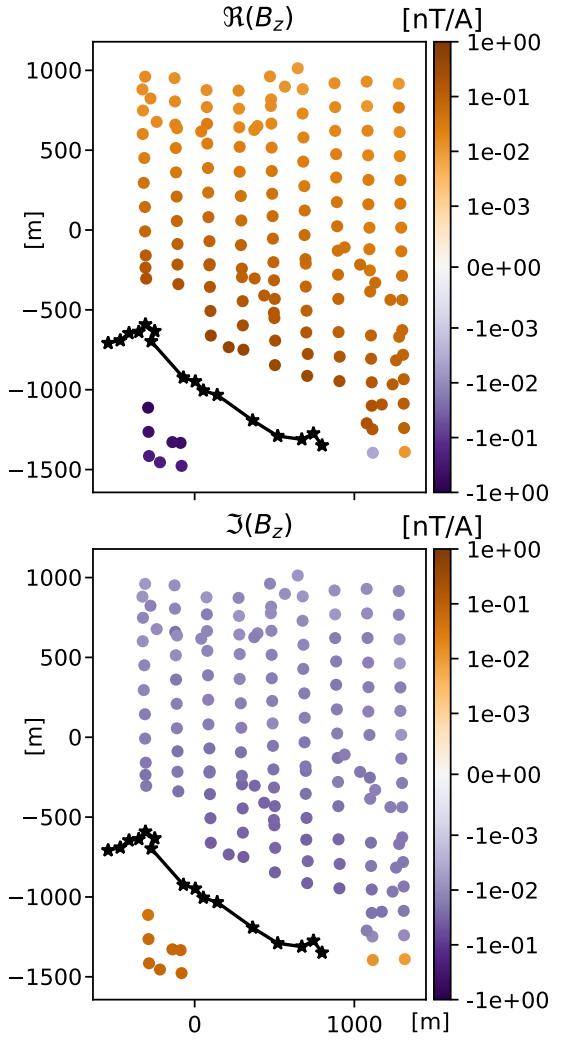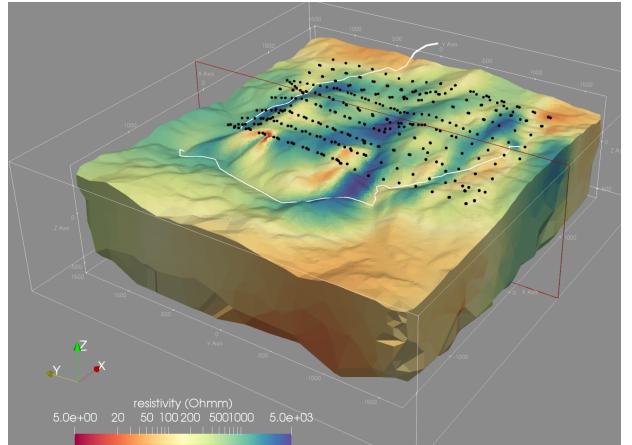
RESULTS

Figure 3: Tx (lines) and Rx positions (dots) of the six overlapping flight area, the Rx colors match the corresponding Tx.

In total, we covered a common measurement area of approximately $1.6\,\text{km} \times 2.6\,\text{km}$. Within all six flight areas, we recorded scalar as well as vector data for three different Tx (Figure 3), using a $100\,\%$ duty cycle signal with base frequencies of $1\,\text{Hz}$ and $32\,\text{Hz}$. Figure 4 provides an example of processed data. Here, we illustrate the real and imaginary parts of the vertical transfer function of the VM data at $256\,\text{Hz}$. The good consistency of the data holds in general. Nevertheless, the horizontal components of the VM data contain segments of poor data quality which are related to locations of sign reversals. Here, we added relative errors of $5\,\%$ to an absolute noise floor of $2\,\text{pT/A}$ for both Rx types and excludes data points with more than $100\,\%$ relative error afterwards. With this procedure we eliminated data within the noise level from the inversion. With $\Re$ and $\Im$ parts, in total $20\,\text{k}$ data points were used for the joint inversion.

We performed multiple inversion runs for both, the individual data sets and jointly, to optimize the mesh and regularization parameters. In the final version, we use a tetrahedral mesh with comparatively small triangles (max. $400\,\text{m}^2$) at the surface to adequately represent the rough topography and a volume constraint of $500{,}000\,\text{m}^3$ to allow smaller conductors to evolve. This setup results in $236\,\text{k}$ cells (model parameters). The regularization parameter λ was 1, decreasing by a factor of 0.8 in each iteration. The 3D view of the final inversion results in Figure 5 shows overall alternating conductive and resistive structure which follow the regional geological strike direction.
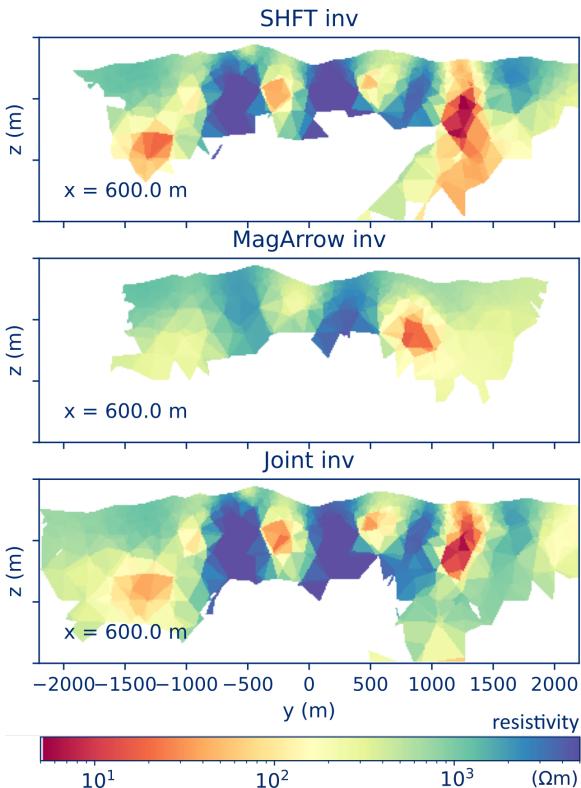

Figure 4: Data example: Vertical component of VM @256 Hz for Tx1.

Figure 5: 3D view of joint inversion result, white lines at surface: Tx, black dots: Rx, frame refers to the location of the slice in Figure 6.

The joint inversion converged from a χ^2 value of 21 down to 1.2. The individual runs of SM and VM data resulted in final χ^2 of 1.08 and 1.22, respectively. Figure 6 presents the recovered resistivity model along a slice perpendicular to the strike direction through the center of the 3D model. In this visualization, we used a coverage threshold (scaled by cell sizes and model parameters) of 1e-5 to avoid displaying features which are most likely effects of the regularization rather than covered by data.

The results indicate four individual and comparatively small conductive structures at different depths from the surface down to maximum 1 km. By analyzing more slice towards East and West, it becomes evident that the recovered conductors match well with the regional geological strike direction. The model recovered from the VM data only exhibits great similarities with the joint inversion. Inverting only the SM data at lower frequencies leads to a generally similar result, but with smoother contrasts. In addition, we observe that the two individual conductors at around y=1000 m in Figure 6 are merged to a single anomaly, indicating a higher equivalence.

Figure 6: Cross section through inversion results, top: three-component VM data only, center: SM data only, bottom: joint inversion of both data sets; only cells with a scaled coverage of >1e-5 are displayed.

Discussion

The SM data yield a lower coverage compared to VM data, even though lower frequencies are accessed. We attribute the smaller coverage of the individual SM data inversion and the dominance of the VM data in the joint inversion to the different amount of data used (1 vs. 3 independent observations at each Rx position and Tx). It would be possible to increase the influence of the SM data artificially by using a higher weighting factor, but we don't see any physical justification for such a modification. Instead, we are confident that robust data error estimates for our SM and VM data (and any other Rx sensors in general) calculated during the processing are the best option to weight our data sets and points properly. The development of such error estimates is work in progress. Even though not presented here, the fit of the final SM response for the individual and joint inversion is almost identical. This observation, the lower coverage of the SM and generally smoother inversion results indicates a higher model equivalence compared to the VM. It is to discussion if doubling the measurement time with two receiver systems is worth the efforts considering the limited contribution of the SM to the final recovered resistivity distribution. However, we present only a single case here and other targets could lead to different observations.

Conclusion

We performed UAV-based semi-airborne electromagnetic measurements in a mostly inaccessible active mining area. The VM data recorded was more suited to resolve the conductivity structure in detail down to more than 500 m depth using three-component data with frequencies between 32 and 756 Hz. The SM data with a good signal quality between 1 and 64 Hz showed in general similar capabilities to recover the subsurface resistivity structure, but with less resolution. The joint inversion results were dominated by the VM data. Against expectations due to the lower frequencies involved, we did not observe deep structures only recovered with the SM data in this study area. However, only by adding these data it was possible to recover the bottom of a deep conductor using joint inversion. Using both receiver types and performing a joint inversion can effectively increase the model robustness and support the interpretation of conductive targets in mineral exploration and beyond. The development of novel vector magnetic field sensors sensitive at low frequencies in combination with an adequate motion noise compensation could significantly contribute to enhance the presented measurement concept.

Acknowledgments

REFERENCES

Abubakar, A., Li, M., Pan, G., Liu, J., & Habashy, T. (2011). Joint mt and csem data inversion using a multiplicative cost function approach. *Geophysics*, *76*(3), F203–F214.

Bastani, M., & Joahansson, H. (2022). A new data acquisition system for uav-borne vlf-lf measurements. two case studies in sweden. In *Nsg2022 3rd conference on airborne, drone and robotic geophysics* (Vol. 2022, pp. 1–5).

Becken, M., Kotowski, P. O., Schmalzl, J., Symons, G., & Brauch, K. (2022). Semi-airborne electromagnetic exploration using a scalar magnetometer suspended below a multicopter. *First Break*, *40*(8), 37–46.

Becken, M., Nittinger, C. G., Smirnova, M., Steuer, A., Martin, T., Petersen, H., et al. (2020). Desmex: A novel system development for semi-airborne electromagnetic exploration. *Geophysics*, *85*(6), E253–E267.

Commer, M., & Newman, G. A. (2009). Three-dimensional controlled-source electromagnetic and magnetotelluric joint inversion. *Geophysical Journal International*, *178*(3), 1305–1316.

Grayver, A. V., Streich, R., & Ritter, O. (2013). Three-dimensional parallel distributed inversion of csem data using a direct forward solver. *Geophysical Journal International*, *193*(3), 1432–1446.

Günther, T., Rücker, C., & Spitzer, K. (2006). Three-dimensional modelling and inversion of DC resistivity data incorporating topography − II. Inversion. *Geophysical Journal International*, *166*(2), 506-517.

Kotowski, P. O., Becken, M., Thiede, A., Schmidt, V., Schmalzl, J., Ueding, S., et al. (2022). Evaluation of a semi-airborne electromagnetic survey based on a multicopter aircraft system. *Geosciences*, *12*(1), 26.

Mackie, R., Watts, M. D., & Rodi, W. (2007). Joint 3d inversion of marine csem and mt data. In *Seg international exposition and annual meeting* (pp. SEG–2007).

Mogi, T., Kusunoki, K., Kaieda, H., Ito, H., Jomori, A., Jomori, N., et al. (2009). Grounded electrical-source airborne transient electromagnetic (GREATEM) survey of Mount Bandai, north-eastern Japan. *Exploration Geophysics*, *40*(1), 1–7.

Rochlitz, R., Becken, M., & Günther, T. (2023). Three-dimensional inversion of semi-airborne electromagnetic data with a second-order finite-element forward solver. *Geophysical Journal International*, *234*(1), 528–545.

Rücker, C., Günther, T., & Wagner, F. (2017). pyGIMLi: An open-source library for modelling and inversion in geophysics. *Computers & Geosciences*, *109*, 106–123.

Vilhelmsen, T. B., & Døssing, A. (2022). Drone-towed controlled-source electromagnetic (csem) system for near-surface geophysical prospecting: on instrument noise, temperature drift, transmission frequency, and survey set-up. *Geoscientific Instrumentation, Methods and Data Systems*, *11*(2), 435–450.

Wu, J., Zhi, Q., Li, X., Chen, X., Li, B., Huang, Y., et al. (2023). Loop source semi-airborne TEM system and its application in landslide detection. *Chinese Journal of Geophysics*, *66*(4), 1758–1770.

Wu, Q., Li, D., Jiang, C., Ji, Y., Wen, Y., & Luan, H. (2019). Ground-source airborne time-domain electromagnetic (gatem) modelling and interpretation method for a rough medium based on fractional diffusion. *Geophysical Journal International*, *217*(3), 1915–1928.